Optimization of the internal structure of 3D-printed components for architectural restoration
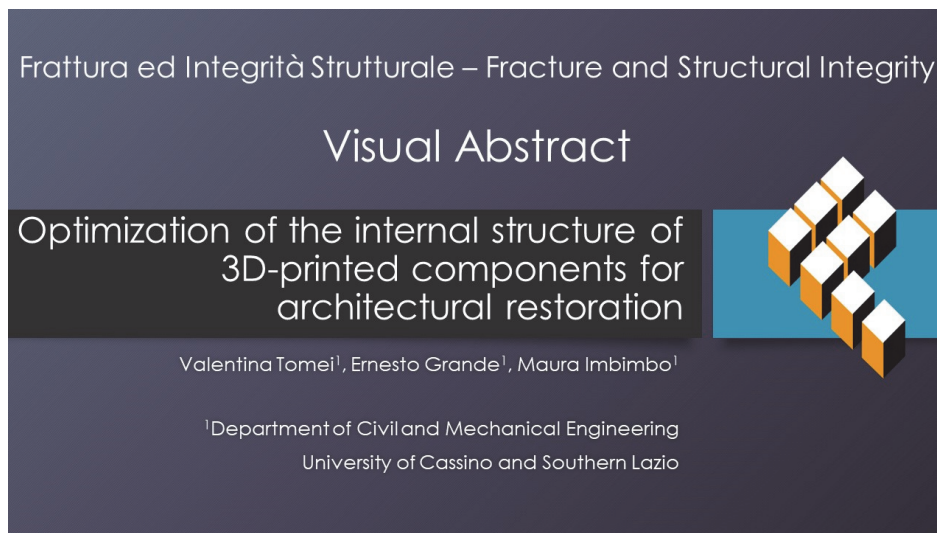
Valentina Tomei, Ernesto Grande, Maura Imbimbo

Department of Civil and Mechanical Engineering. University of Cassino and Southern Lazio, Italy.
v.tomei@unicas.it, http://orcid.org/0000-0002-3063-7702
e.grande@unicas.it, https://orcid.org/0000-0002-3651-1975
m.imbimbo@unicas.it, https://orcid.org/0000-0003-3163-3073

Frattura ed Integrità Strutturale – Fracture and Structural Integrity

Visual Abstract

Optimization of the internal structure of 3D-printed components for architectural restoration

Valentina Tomei[1], Ernesto Grande[1], Maura Imbimbo[1]

[1]Department of Civil and Mechanical Engineering
University of Cassino and Southern Lazio

INTRODUCTION

The capacity to reproduce complex geometries in short times and the possibility of using different types of materials (among these, also, eco-sustainable ones), make 3D-printing a technology with great potential for applications in different fields, among which architecture and construction [1]. Among these, applications concerning the recovery of structural heritage are one of the most recent fields of particular interest. Indeed, examples proposing the use of 3D-printing for the reproduction of small museum components [2], or the reproduction of missing parts of ancient statues [3] are available in current literature. Other examples concern the reproduction of ornamental architectural components [4], among which the Roman cornice from the Castulo Archaeological Site [5], or the restoration of an ancient terra sigillata plate [6].

In contrast to applications for mechanical devices, which often necessitate specific strength and stiffness characteristics for 3D-printed components, the recovery of architectural/ornamental elements prioritizes refinement of the exterior surface

and shape precision. Consequently, optimizing the internal structure configuration is crucial in this context. It enables, indeed, to reduce weight, fabrication costs and environmental impact, as well as to minimize the intrusiveness of connecting the 3D-printed element to the structure, a further important aspect for historical structures.

The application of 3D printing for reproducing architectural/ornamental components is currently under study, with a main focus of characterizing the performance of printed materials [7]–[15]. The parameters of the printing process intrinsically affect the mechanical properties of the printed parts. Therefore, experimental characterization of samples represents a crucial preliminary phase that supports the design process of complex elements derived from 3D printing.

In this study, we present both experimental and numerical investigations aimed at assessing the structural performance of 3D printed elements made of PLA material. Initially, the focus is on characterizing the printed material through tensile tests on dog-bone samples. Subsequently, bending tests were conducted on plate samples representing small portions of 3D-printed elements with different internal structure configurations derived from numerical optimization techniques. Additionally, the paper discusses results obtained from theoretical models and Finite Element analyses, providing further insights into the experimental findings.

MATERIALS AND METHODS

The samples for the experimental tests presented in this paper were manufactured by using additive manufacturing (AM) technology based on the fused filament technique (FFT). The black RAISE3D Premium PLA material was used, with the following main printing parameters set:
- filaments diameters: 1.75 mm;
- minimum/maximum printing temperature of 190°C/220°C;
- nozzle diameter: 0.4 mm;
- layer thickness: 0.25 mm;
- layer width: 0.5 mm;
- infill value: 100%;
- nozzle speed: 50 mm/s;
- hot-end temperature: 190°C.

The selection of the PLA material was primarily based on its advantages over other common 3D printing materials, such as: biodegradability, eco-sustainability, recyclability, low extrusion and bed temperatures, reduced risk of ultrafine particle emission during printing [16]–[18]. However, the mechanical properties of 3D-printed elements made of PLA material are strongly influenced by various printing parameters (extrusion temperature, flow rate, layer height, and direction) and by the printing process itself [17]. Then, the study presented here further contributes to the state of the art regarding this aspect. To this specific end, dog-bone samples were indeed experimentally analyzed by performing tensile tests finalized to characterize the materials in terms of Young Modulus E and strength in terms of stress σ_{lim}.

Moreover, the study experimentally and numerically analyzes the influence of the configuration and the pattern of the internal structure of 3D-printed samples representative of components or parts of more complex ornamental elements. For this purpose, plate samples underwent preliminary experimental analysis through three-point bending tests. Subsequently, numerical results were derived by using simple theoretical models and Finite Element analyses. As detailed in the following section, plate samples were printed with varying internal structure configurations (reticular and rhomboidal) and patterns (determined by different inclinations of internal walls).

The same printing process was applied to both dog-bone and plate samples. Specifically, for each layer composing the sample, the perimeter was initially printed by following a linear path, while the inner area was subsequently printed by following an inclined path at an angle of ±45° alternately for each successive layer (Fig. 1). In the case of dog-bone samples, a temporary support was required during the printing process (Fig. 1b).

DESIGN OF THE INTERNAL STRUCTURE OF THE PLATE SAMPLES

Plate samples were designed with two distinct configurations of the internal structure: reticular and rhomboidal, labeled as PR and PT, respectively. For each configuration, two different patterns, primarily distinguished by varying the inclination θ of the walls forming the internal structure, were also taken into account. These patterns are denoted as PR_60 and PR_72 for the reticular pattern, and PT_27 and PT_45 for the rhomboidal pattern. (Fig. 2).
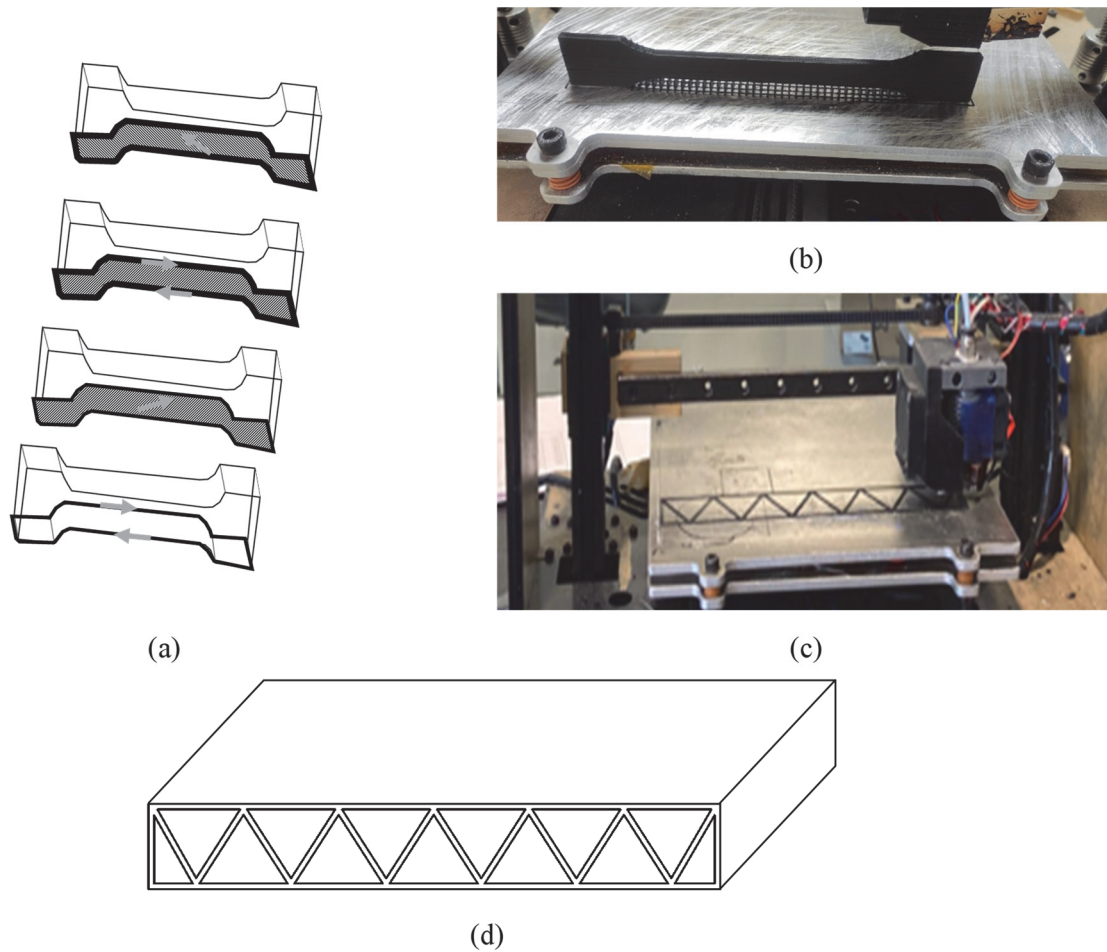
Figure 1: 3D-printing process: (a) disposition of layers; (b) dog-bone sample; (c) plate sample during the printing process; (d) axonometric view of a plate sample. .

Concerning the reticular configuration, the two distinct patterns were defined by interior walls inclined at ±60° (PR_60) and interior walls inclined at ±72° (PR_72). Both configurations maintained an identical thickness for both the flanges and the walls. (Fig. 2; Tab. 1).

Regarding the rhomboidal configuration (Fig. 2; Tab. 1), the internal walls were arranged to create a rhomboidal mesh. Specifically, the two distinct patterns considered were distinguished by walls inclined at 27° (PT_27) and, for the other type of sample, walls inclined at 45° (PT_45).

For each configuration (reticular and rhomboidal), the two pattern were derived from an optimization design process relied on a parametric geometrical model (Fig. 3c) created in Grasshopper [19], [20], along with a corresponding structural model developed in Karamba3D [21].

In detail, for the reticular pattern the problem was set as in the following:

- ✓ constraint conditions: the structural optimization process was carried out by imposing a constraint condition on the maximum utilization ratio, denoted as $U_{max}=\sigma_{VM}/\sigma_{lim}\leq 1$, where σ_{VM} represents the maximum value of Von Mises stress, considering the average strength value deduced from tensile tests on dog-bone samples (σ_{lim} =44 MPa);
- ✓ parameters: regarding the parameters varied during the optimization process, the PR_60 solution was obtained by adjusting both the slope θ of the internal structure walls and the thickness t (with the latter assumed to be the same for both walls and flanges). On the other hand, the PR_72 solution was derived by varying only the slope θ, while setting the thickness obtained for PR_60. This choice was made to compare structural models with the same thickness.

About the rhomboidal configuration, the optimization process was set as in the following:

- ✓ constraint conditions: the structural optimization process was carried out by imposing as the main constraint condition the same volume of material of the pattern PR_60 of the reticular configuration, in order to compare

different solutions with the same volume (the values of volumes and masses of the samples are reported in Tab. 1). Furthermore, considering the average strength value deduced from tensile tests on dog-bone samples (σ_{lim} =44 MPa), an additional constraint was imposed on the maximum utilization ratio, denoted as $U_{max}=\sigma_{VM}/\sigma_{lim}\leq 1$, where σ_{VM} represents the maximum value of Von Mises stress;

✓ parameters: regarding the parameters varied during the optimization process, the PT_27 solution was obtained by adjusting both the slope θ of the internal structure walls and the thickness t (with the latter assumed to be the same for both walls and flanges). On the other hand, the PT_45 solution was derived by varying only the thickness t, while setting the slope θ to 45°.
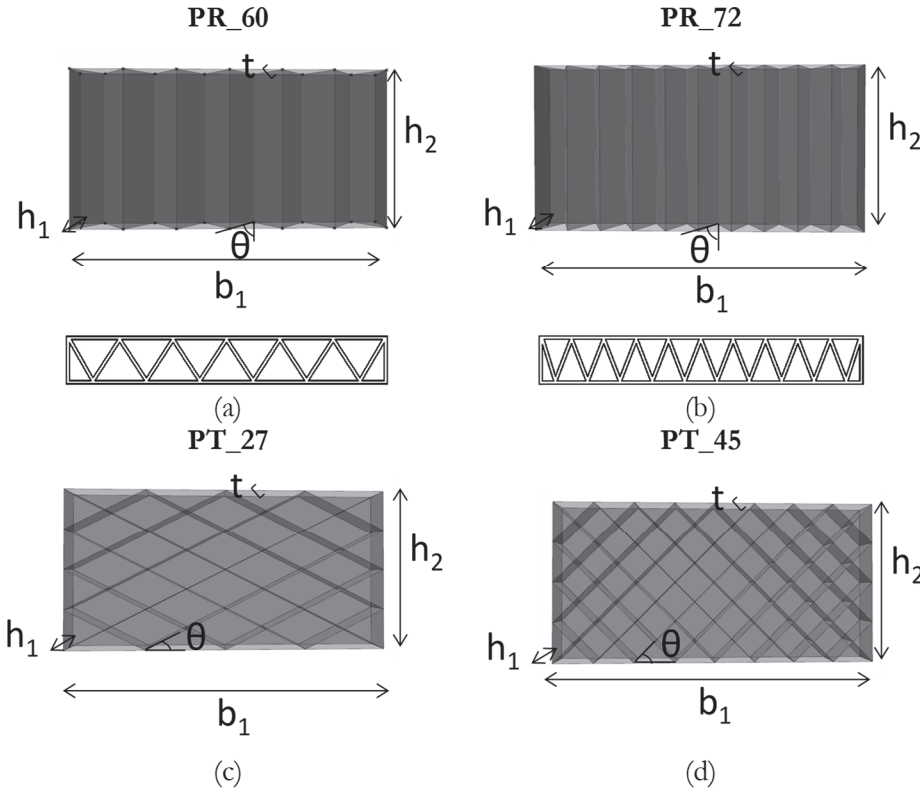

Figure 2: Geometry of the reticular samples (a) PR_60 and (b)PR_72, and the rhomboidal samples (c) PT_27 and (d) PT_45.

	b_1 (mm)	b_2 (mm)	h_1 (mm)	h_2 (mm)	r (mm)	t (mm)	θ (°)	n. of samples	Volume (cm²)	Mass (g)
DB	150	80	20	10	20	4	-	5	-	-
PR_60	200	-	30	100	-	4	60	5	399	498
PR_72	200	-	30	100	-	4	72	5	437	546
PT_27	200	-	30	100	-	4	27	5	399	498
PT_45	200	-	30	100	-	3.5	45	5	399	498

Table 1: Dimensions, volumes and masses of the samples.

The numerical analyses conducted during the optimization process simulated the experimental three-point bending test described in the paper (Fig. 3), where the span was set at s=10 cm and a uniform load was distributed along the centerline of the upper flange (the resultant of this load being the total applied force F).

The optimization problem was tackled by using mono-objective genetic algorithms, defining the following objective function OF to be maximized (Eq. 1):

$$OF = F + \alpha \left| V - V^* \right| + \beta \tag{1}$$

where α is a penalty factor, assumed here to be -10⁵, and β is a parameter introduced to adhere to the constraint condition of the utilization ratio (it takes a value of -10⁵ when $U_{max}>1$ and 0 when $U_{max}\leq 1$). Here, V and V* represent respectively the

volume of material of the reticular solution PR_60 (taken as the reference value) and the volume obtained during the optimization process. The developed visual script is depicted in Fig. 3c, outlining all the main steps.

Details regarding the dimensions of the plate sample are presented in Tab. 1, with the symbols referring to Fig. 3.
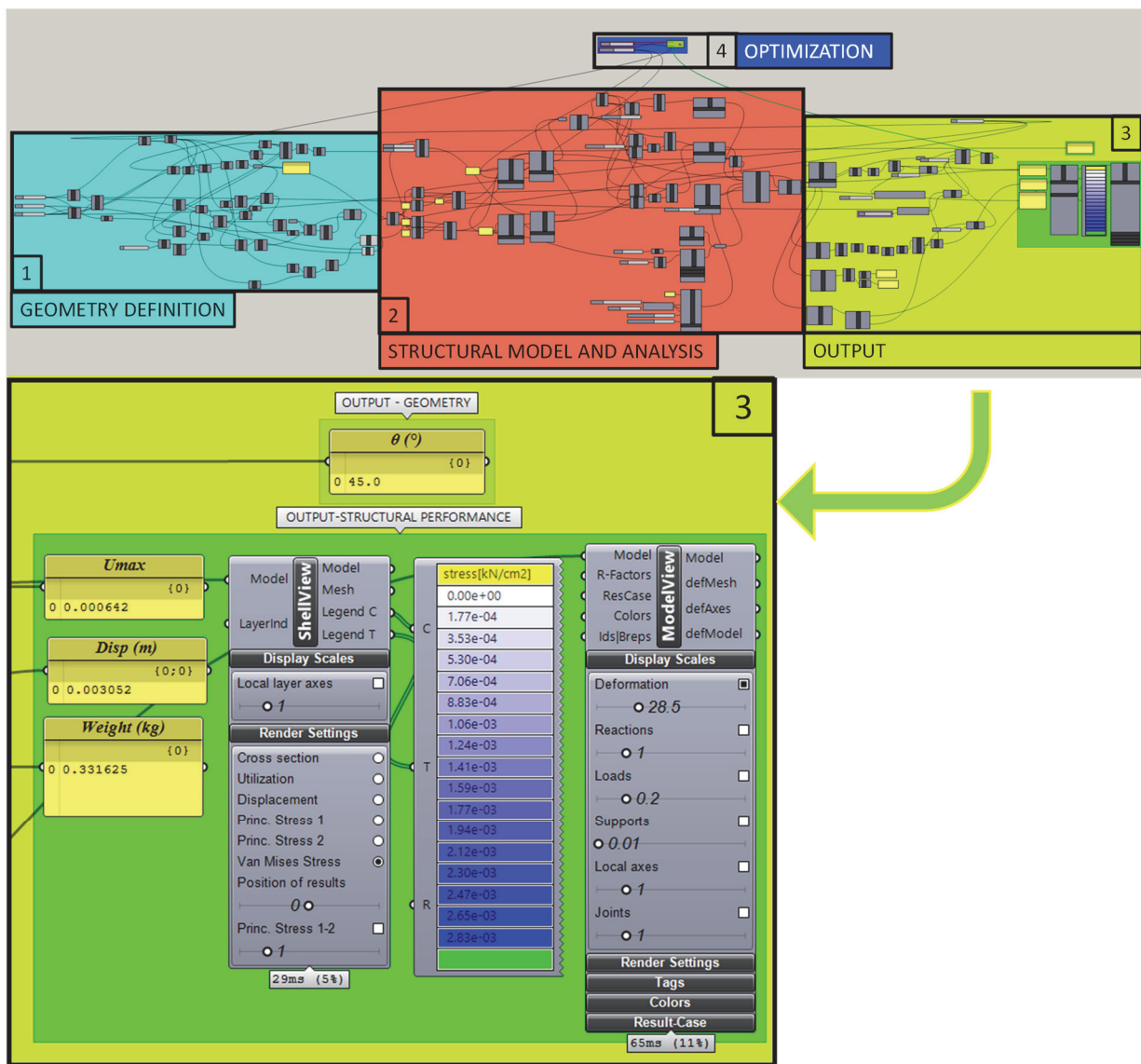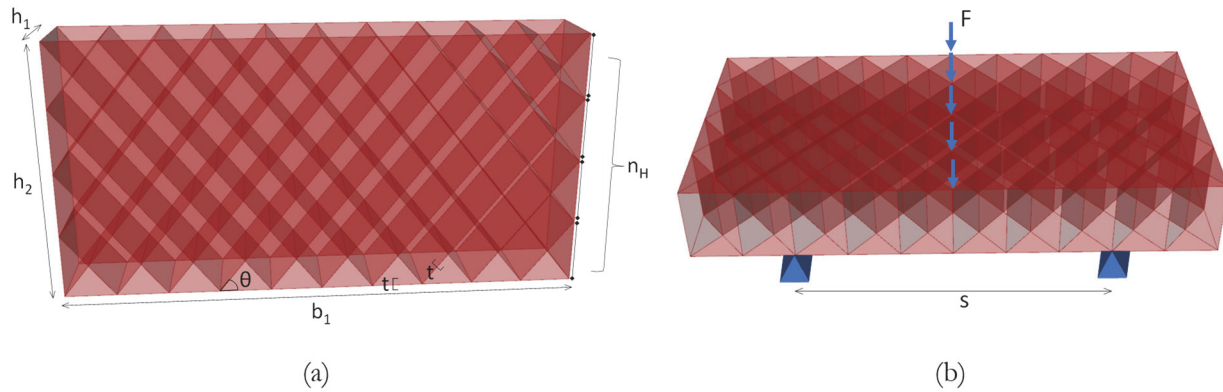

Figure 3: (a) parametric model of the rhomboidal pattern (PT); (b) structural model employed for optimization ; (c) visual script developed in Grasshopper Environment.

EXPERIMENTAL TESTS

Dog-bone samples: material characterization

The initial phase of the experimental work aimed to explore the behavior of the printed material. For this purpose, tensile tests were conducted on five samples, each featuring a common dog-bone shape (DB, see Fig. 4 and Tab. 1). Tensile tests on DB samples were performed at the University of Cassino and Southern Lazio by using a universal testing machine Gabaldini (Fig. 5).
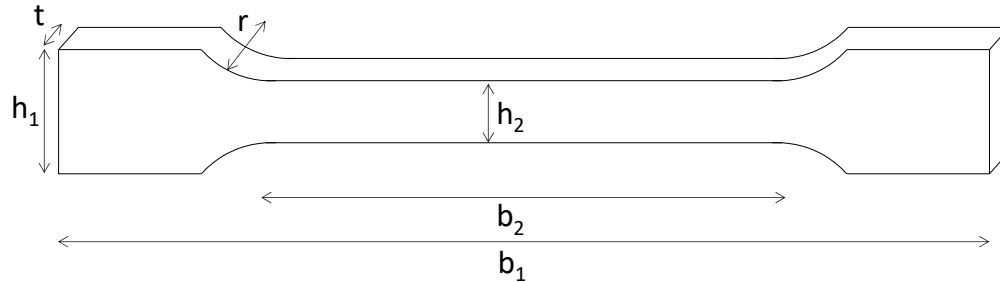

Figure 4: Geometry of the dog-bone samples.

The results derived from the tensile tests on DB samples are depicted in Fig. 6 in terms of stress-strain curves. Here, the stress was calculated by dividing the applied force by the cross-sectional area of the sample, while the strain was determined by dividing the displacement by the length of the sample. From the plots, it is evident that all the samples exhibit an initial linear phase followed by a post-peak behavior characterized by a softening branch. An average elastic modulus value E=1250 MPa (evaluated at 40% of the peak stress) and an average peak stress value σ_{lim}=44 MPa were deduced from the tensile tests. Despite the similar overall force-displacement response of the samples, it is noticeable from the plots that one of the samples exhibits lower strength and stiffness values, along with greater ductility. This divergent behavior of the sample may be attributed to potential and inevitable misalignments during the test and, moreover, to geometric imperfections arising during the printing process [22], [23].

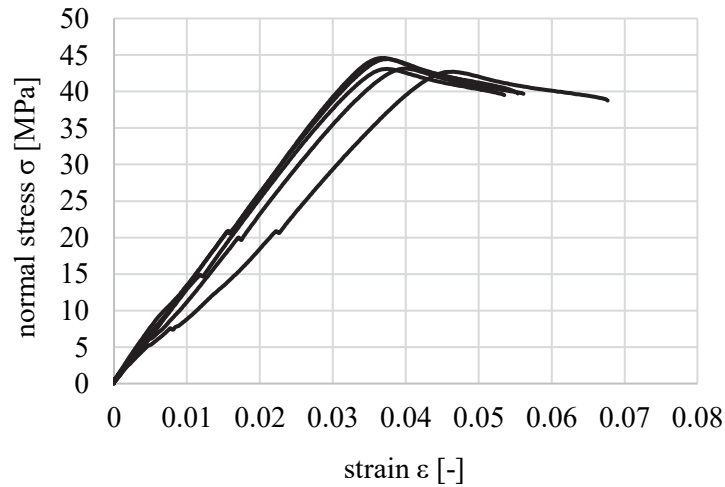Figure 5: Tensile tests on reticular beams: picture of the testing machine.

Figure 6: Tensile tests on dog-bone samples: stress-strain curves.

Fig. 7 shows pictures of the DB samples at the conclusion of the tests. From the figure, it is evident that all the samples exhibit a characteristic fracture near the center of the sample.
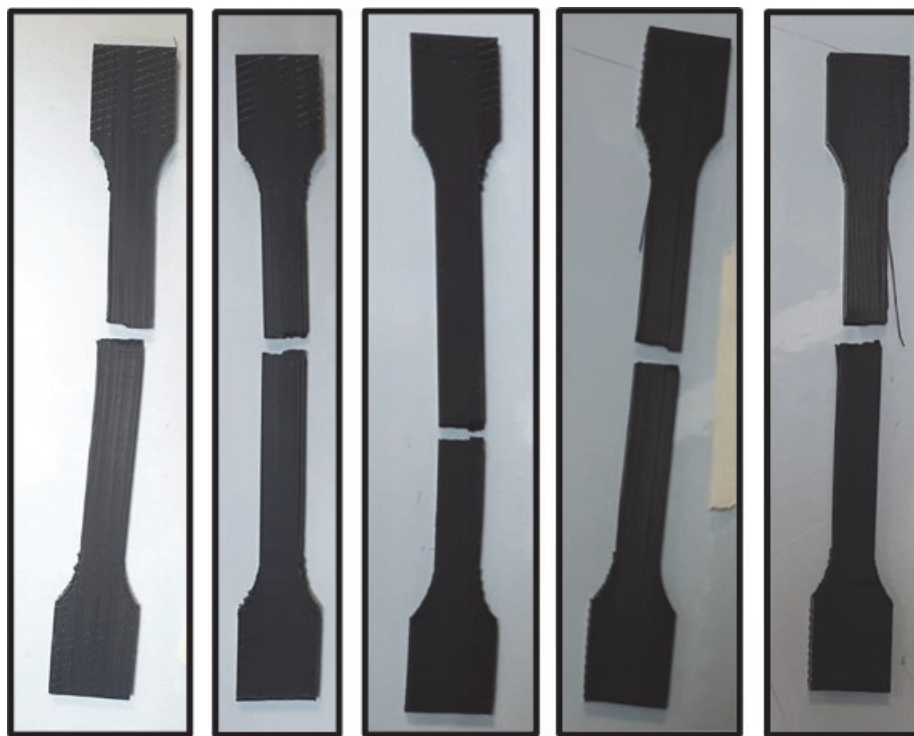

Figure 7: Tensile tests on dog-bone samples: failure modes.

Plate samples: structural characterization

Regarding the plate samples, three-point bending tests were performed at the laboratory of Pa.L.Mer. in Ferentino (FR), Italy.

The results obtained from the three-point bending tests on plates are illustrated in Fig. 8, in terms of Force-Displacement curves. Specifically, Fig. 8a compares the two patterns of the reticular configuration, while Fig. 8b contrasts the two patterns of the rhomboidal configuration.

Regarding the reticular configuration, Fig. 8a shows that the PR_72 samples exhibit higher peak force and corresponding displacement values compared to the PR_60 samples. However, the differences are relatively small, approximately 10% in

terms of peak force and 20% in terms of corresponding displacement (evaluated based on the average values). Conversely, both types of samples demonstrate similar initial stiffness values.

On the other hand, concerning the plates with the rhomboidal configuration, it is noticeable that the PT_27 samples demonstrate higher values of both stiffness and strength compared to the samples with the PT_45 pattern. Conversely, the two patterns yield similar values of the displacement at the peak. Comparing the two configurations (reticular and rhomboidal), it is evident that both patterns of the rhomboidal configuration (PT_27 and PT_45) exhibit higher values of both peak force and corresponding displacement compared to the two patterns of the reticular configuration (PR_60 and PR_72). Given that the samples PR_60, PT_27, and PT_45 have the same weight, these results clearly highlight the influence of the pattern on the structural performance of the samples.

Examining the failure modes of the reticular plates depicted in Fig. 9, similar failure modes are evident for the PR_60 and PR_72 patterns, where cracks occurred in both flanges without affecting the internal walls. In contrast, for plates with the rhomboidal pattern, cracks involved both flanges and walls. The inclusion of internal walls in the failure of the rhomboidal plates likely contributes to the higher load attained compared to reticular plates.
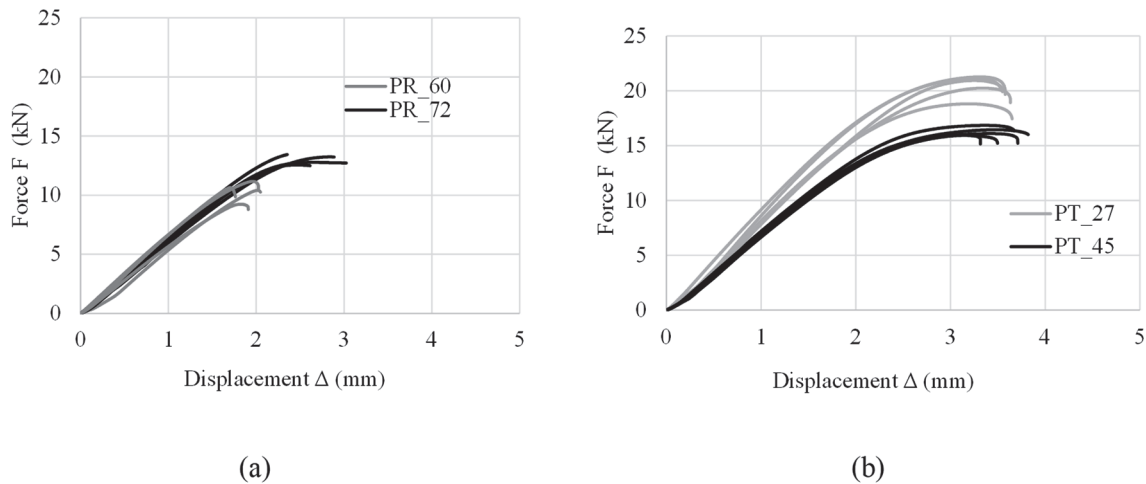

(a)

(b)

(c)

Figure 8: Three-point bending on reticular plates: Force-Displacement curves for plates PR (a); plates PT (b); picture of the testing machine (c).
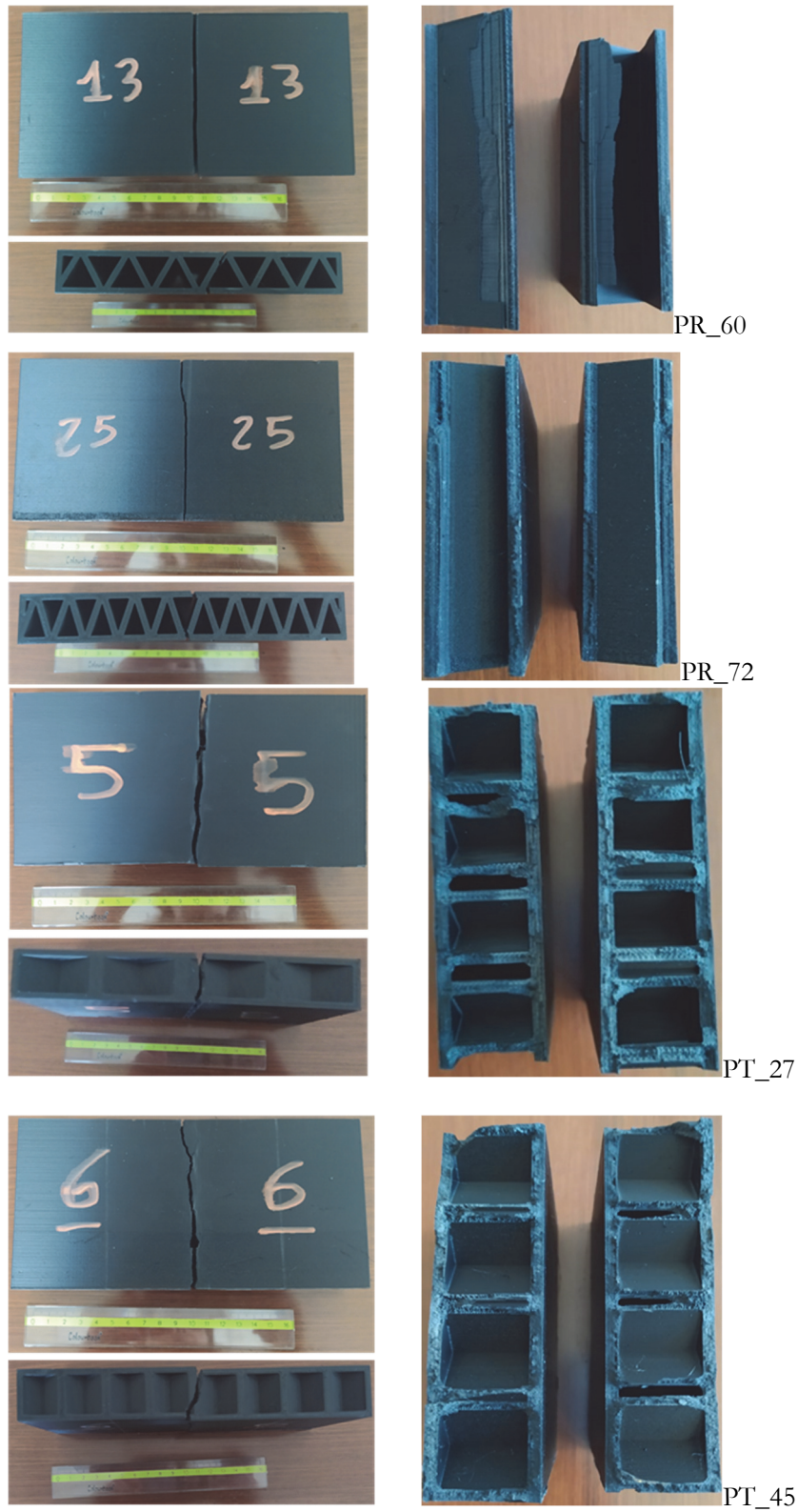
Figure 9: Three-point bending on reticular plates: failure modes.

NUMERICAL F.E. ANALYSES

Numerical analyses replicating the experimental bending tests were conducted using the computer code Abaqus [24]. A 3D model was carried out by employing thin shell elements for both flanges and internal walls. Regarding the constitutive law, unlike the linear static analyses utilized in the optimization design, nonlinear static incremental analyses were performed. For this purpose, a constitutive material law was adopted, based on the findings from the tensile tests on dog-bone samples. This law featured an initial linear-elastic branch with a Young's modulus E of 1250 MPa until reaching the peak stress (σ_{lim} = 44 MPa), followed by a softening branch with a slope determined by considering an ultimate strength value of 40 MPa and a corresponding strain value of 0.055 was implemented.

The developed structural model was employed for analyzing the influence of the internal pattern on the attainment of the material normal stress limit. The results of the numerical analyses are presented below in terms of force-displacement curves, with a circular symbol denoting the point at which the material yields.

The comparison between experimental and numerical curves (Fig. 10) underlines:

✓ a good agreement in terms of initial bending stiffness for both configurations, indicating the appropriateness of assuming an isotropic material model and the value of the Young's modulus derived from tensile tests on dog-bone samples;

✓ for the reticular configuration, an overestimation of the plate's performance in terms of peak load is evident from Fig. 10 a and b, indicating that the failure is not governed by the attainment of the maximum axial stress σ_{lim};

✓ for the rhomboidal configuration, in both patterns PT_27 (Fig. 10c) and PT_45 (Fig. 10d) the numerical attainment of the material's yield strain occurs at similar values of loads and displacement, with the latter approaching the peak value of the experimental load (Fig. 10c).

In Fig. 11 and Fig. 12 are presented the minimum and maximum stresses of samples at the attainment of yielding. From the figures, as expected, is evident the concentration of normal stresses at the middle of flanges, where the failure was experimentally observed.
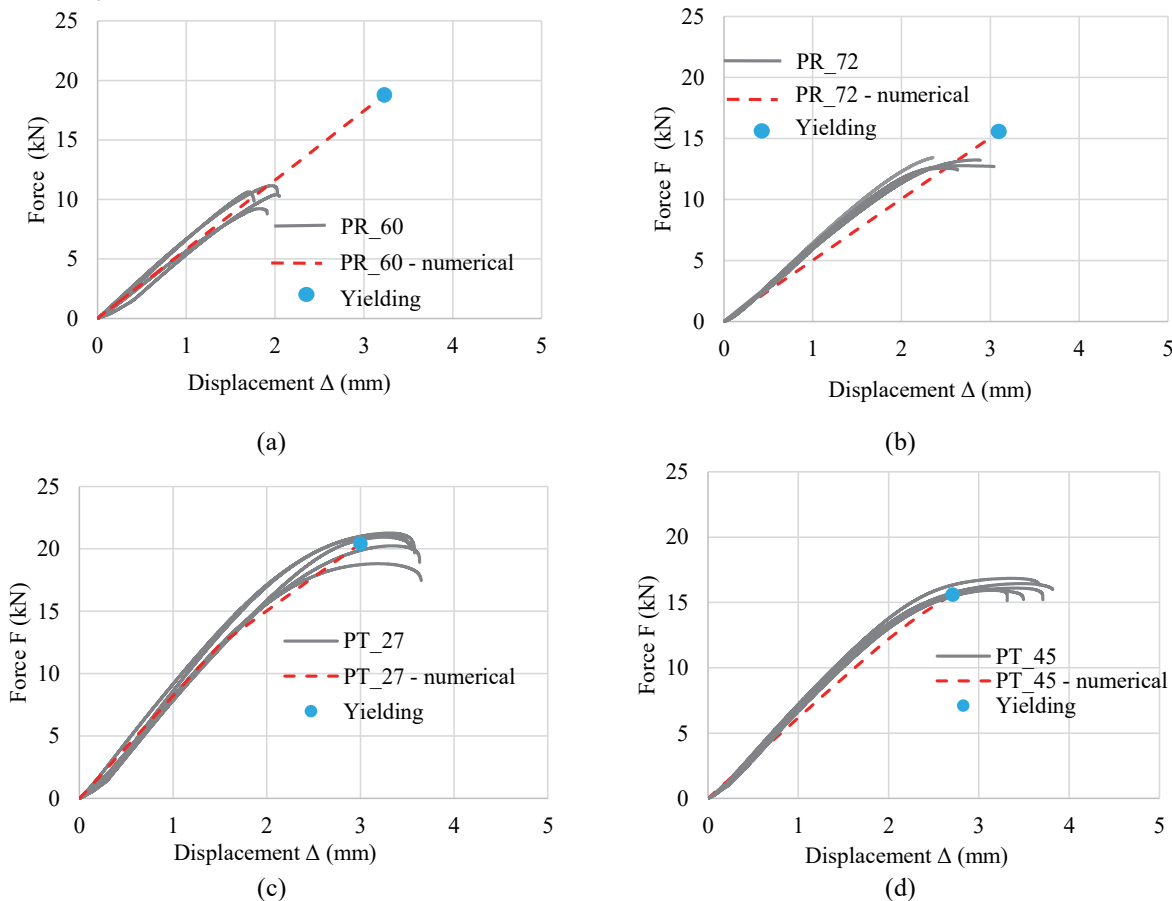

Figure 10: Results of numerical analyses: applied force vs. displacement curves.
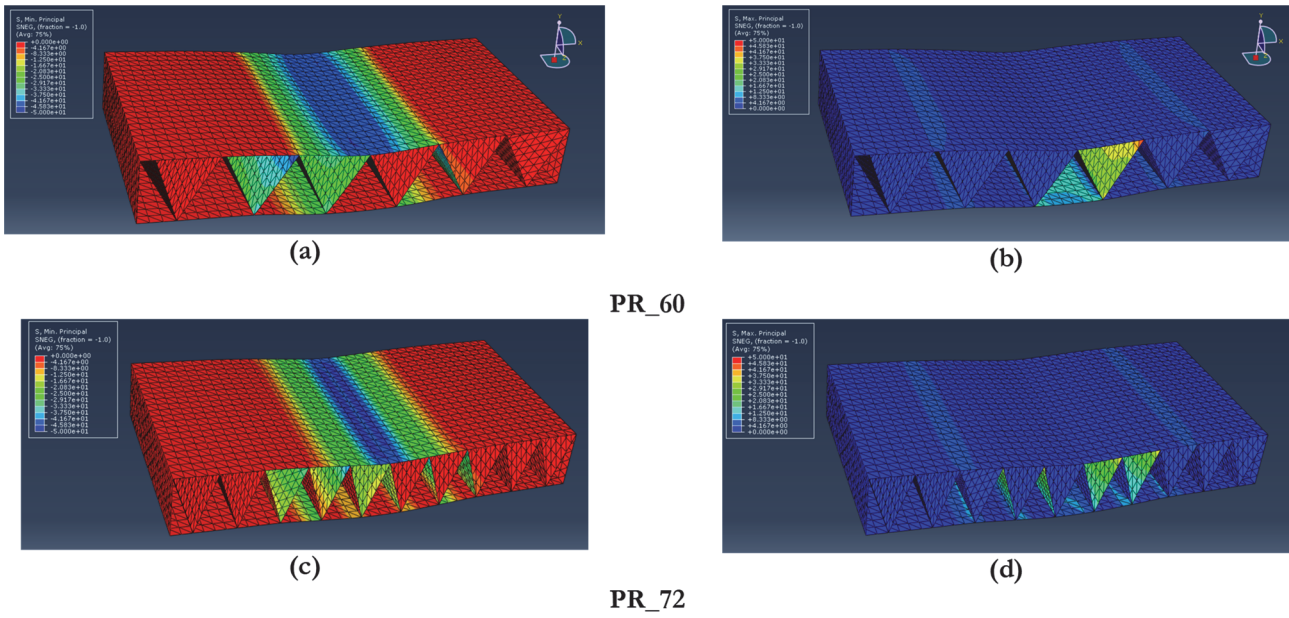
PR_60

PR_72

Figure 11: Non-linear numerical model: minimum (a, c) and maximum (b, d) stresses for PR_60 (a, b) and PR_72 (b) at yielding.
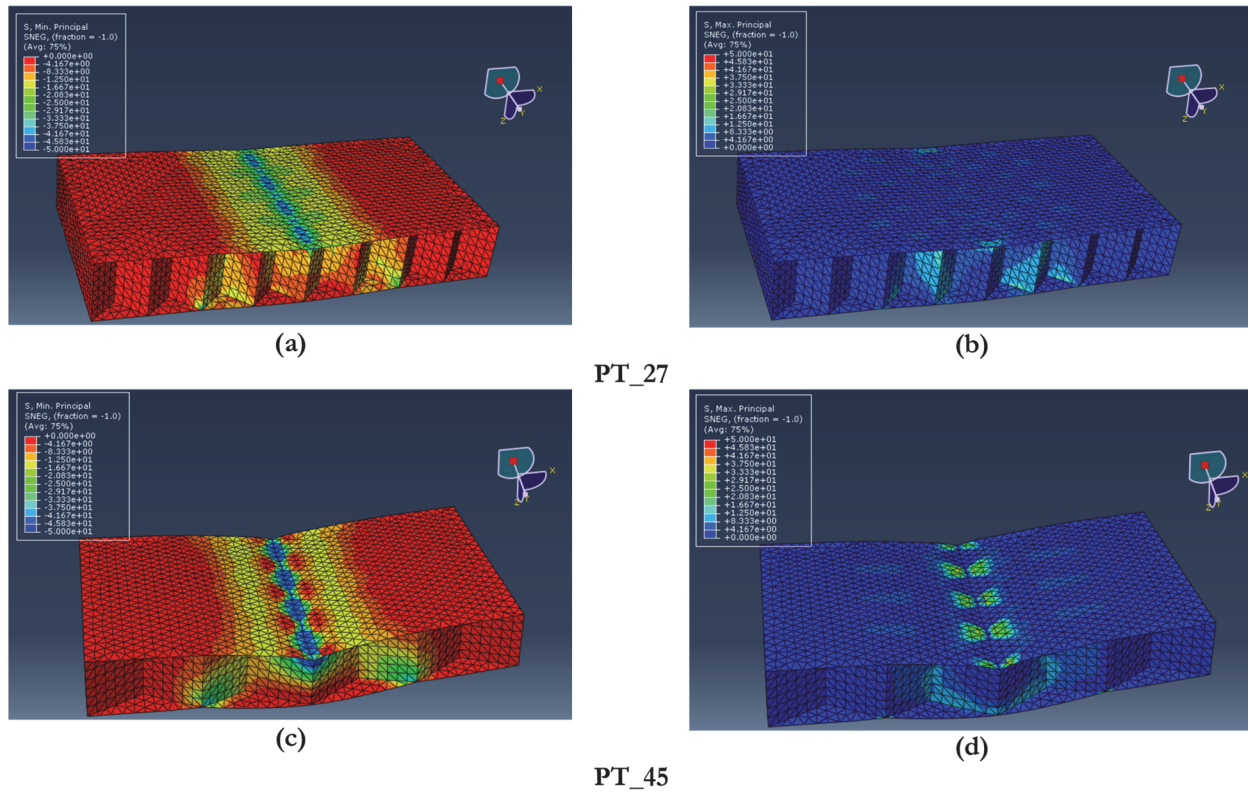

PT_27

PT_45

Figure 12: Non-linear numerical model: minimum (a, c) and maximum (b, d) stresses for PT_27 (a, b) and PT_45 (c, d) at yielding.

CONSIDERATIONS

The results obtained from the experimental tests presented above have highlighted the influence of both configuration and pattern on the flexural response of samples.

However, the F.E. numerical analyses have indicated that, in some cases, reaching the limit normal stress corresponds to significantly higher levels of load than those determined experimentally.

To deepen these aspects, considerations carried out through simple models, mainly based on equilibrium considerations and assumptions concerning the failure mode, are reported in the following.

Beginning with the assumption of a pure shear failure mode involving only the flanges in the case of the reticular configuration, the average value of shear stress τ_p corresponding to reaching the experimental peak load F_{max} is determined by dividing the shear action $S_{p,PR}$ (assumed to be half of the peak load due to the static three-point bending scheme depicted in Fig. 13) by the cross-sectional area of both flanges (the depicted cross-section is shown in Fig. 13b, where $F_{i, PR}$ are the internal forces, d^* is the internal lever arm and M_{PR} is the bending moment). The obtained average shear stress value (6.9 MPa) is then utilized to evaluate the force corresponding to the shear failure of samples with a rhomboidal configuration. In this regard, as the failure modes of rhomboidal samples involve both flanges and internal walls, the shear stress value obtained for reticular samples is multiplied by the cross-sectional area of both flanges and internal walls to obtain the shear force (the depicted cross-section is shown in Fig. 13c, where $F_{i, PT,1}$ are the internal forces related to the flanges, $F_{i, PT,2}$ are the internal forces related to the internal walls, d_1^* and d_2^* are the relevant internal lever arm, and M_{PT} is the bending moment). Consequently, while still considering the three-point static test scheme, the corresponding force is determined by simply doubling the shear force, resulting in a value of 22.5 kN. This obtained value closely aligns with the experimental average peak force of rhomboidal samples (approximately 21 kN), thereby confirming an ultimate behavior for these samples likely governed by a shear failure mode, rather than the attainment of the limit normal stress.
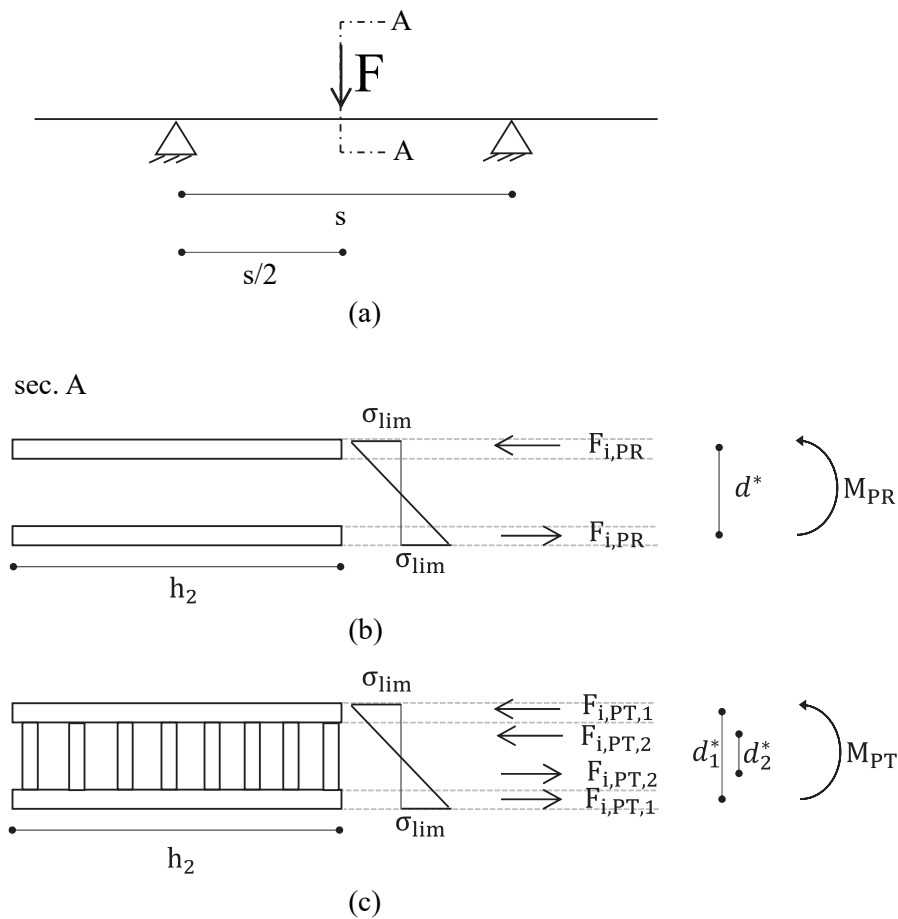

Figure 13: Structural scheme of the samples (a), cross-sectional analysis of reticular samples (b) and rhomboidal samples (c).

Indeed, supposing, on the contrary, a bending failure mode for both reticular and rhomboidal samples (Fig. 13b-c), resulting in the attainment of the limit normal stress σ_{lim} at both exterior edges of the flanges, and assuming a linear material behavior, the corresponding forces are calculated to be 18.6 kN and 23.5 kN for reticular and rhomboidal samples, respectively. The obtained value for reticular plates exceeds the corresponding experimental average values, whereas for rhomboidal plates it approaches the experimental results. This confirms the occurrence of a shear failure mode for reticular plates and a possible balanced shear/bending failure mode for rhomboidal plates.

To further emphasize that shear failure, rather than bending, governs the behavior of plates with a reticular configuration, a simplified evaluation of normal stress in the lower and upper flanges was conducted, considering a pure 2D truss behavior (Fig. 14):

$$\sigma = \frac{F \cdot s}{4 \cdot h_1 \cdot t \cdot h_2} \tag{2}$$

where F is the force level. Then, by utilizing Eqn. (2) and the experimentally derived values of force F for reticular plates, the curves in terms of normal stress σ – displacement Δ shown in the plot of Fig. 14 were obtained. In the same plots, the range of peak normal stress values obtained from tensile tests conducted on DB samples was also included.

From the figure, it is evident that the peaks of the σ-Δ curves are significantly lower than the range of peak stress observed in the DB samples, thereby confirming that bending did not govern the failure for this plate configuration.
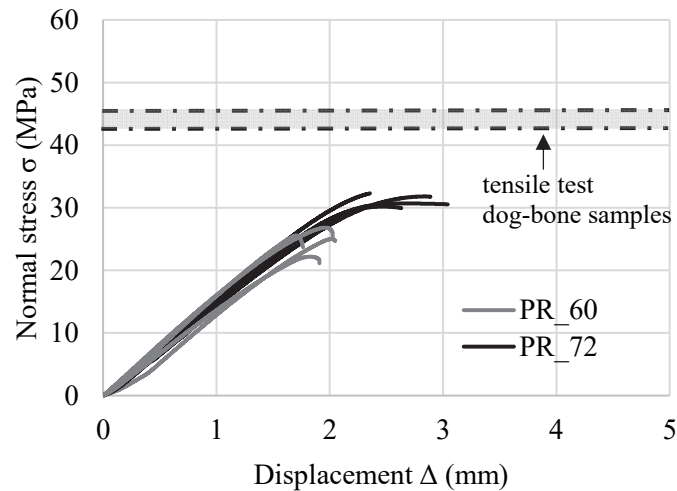

Figure 14: Normal stress-displacement curves for reticular plates PR.

CONCLUSIONS

3D-printing technology is increasingly appealing for architectural and ornamental restoration projects involving historical structures. This technology enables the accurate reproduction of both the exterior surface details and the intricate shapes of the elements to be replicated. It is evident that for such applications, the shape and volume of the 3D-printed element are fixed parameters closely related to the element being restored. However, the amount of material composing the internal volume of the 3D-printed element could be considered the primary parameter to be optimized in a design optimization process. This optimization aims to achieve an internal structure with configurations and patterns that reduce the material usage (thus, fabrication costs and weight), and consequently, minimize the invasiveness of the intervention required to connect the restored element to the structure.

The paper presented here has focused attention on this aspect by experimentally and numerically analyzing the influence of the configuration and pattern of the internal structure of 3D-printed plate elements, which are representative of more complex elements, on their flexural behavior.

Regarding the experimental tests, before presenting the results deduced from the bending tests on the plates, a preliminary material characterization was conducted by performing simple tensile tests on samples with a typical dog-bone shape. The results obtained from these preliminary tests provided valuable information regarding the parameters governing the tensile response (Young's modulus, tensile strength, displacement at the peak) and the tensile behavior of the printed material, characterized by an initial linear phase followed by a softening post-peak phase.

The bending tests conducted on the plates generally exhibited a flexural behavior in terms of applied force-displacement (or stress-displacement) similar to that deduced from the tensile tests on dog-bone samples: an initial linear behavior followed by a nonlinear one with softening before failure, which was particularly evident for the rhomboidal configuration. In this case, the obtained results also emphasized the influence of the configuration/pattern of the internal structure. Particularly for the reticular samples, it was observed that the PR_72 samples, characterized by a greater slope and number of diagonal

walls (and consequently a greater weight), exhibited slightly higher values of strength (peak force) compared to the PR_60 samples. Conversely, for the samples with a rhomboidal configuration of the internal structure, greater strength in terms of force was observed for the samples with the PT_27 pattern, i.e., the one with a lower number of internal walls. This difference was closely related to the fact that the rhomboidal samples were designed to have the same weight, with the PT_27 samples characterized by a greater thickness compared to the PT_45 samples. Another distinction with respect to the reticular configuration concerned the displacement at the peak, which, in the case of the rhomboidal configuration, was similar for both patterns, while slightly different for the reticular ones.

The numerical F.E. analyses, conducted by setting constitutive laws based on those derived from the tensile tests, highlighted a good agreement in terms of both stiffness and strength for the rhomboidal configuration. On the other hand, they exhibited a good agreement in terms of stiffness only for the reticular configuration. Indeed, for the latter, the experimental tests showed a strength lower than the numerical one, indicating that the failure was not due to reaching the limit normal stress. The analyses presented in the paper, derived from simple theoretical models, confirmed this outcome by further emphasizing the influence of the configuration/pattern on the experimental response of printed samples.

The paper contributes to a significant topic within the application of 3D-printing technology for architectural and ornamental restoration, contributing to a broader research initiative. Practical applications of these studies, which focus on small plates, include the reproduction and installation of missing parts of historic buildings with linear walls, an example of which can be the reproduction of missing battlements of monumental structures, as proposed by the Authors within the Italian regional projects: *DTC TE1 - Fase II - Progetti RSI", Det. N. G07413 of 16.06.2021, public notice of LAZIO INNOVA; research project "H-S3D – Stampa 3D per Beni Culturali. Applicazioni di Recupero Strutturale e Monitoraggio di Elementi Architettonici e di Decoro".*

Additionally, the technology facilitates the creation of intricate forms, making it possible to reproduce ornamental elements with ease due to 3D printing's capability to generate complex shapes without technical challenges. In this framework, it is essential to understand the mechanical behavior of these elements, even if they are purely decorative, to ensure they are designed to be self-supporting. Future research will further investigate the role of internal structural configurations of printed elements, considering the complex shape of the elements as an additional parameter in the optimization process.

REFERENCES

[1] Pajonk, A., Prieto, A. and Blum, U. (2022). Multi-material additive manufacturing in architecture and construction: A review. J. Build. Eng., New York, NY, pp. 103603. DOI: 10.1016/j.jobe.2021.103603.

[2] Kantaros, A., Ganetsos, T. and Petrescu, F. I. T. (2023). Three-Dimensional Printing and 3D Scanning: Emerging Technologies Exhibiting High Potential in the Field of Cultural Heritage. Appl. Sci., Basel, Switzerland, pp. 4777. DOI: 10.3390/app13084777.

[3] Almerbati, N. and Dustin, H. (2016). Heritage conservation in the new digital era: The benefits of 3D printing architecture screens in sustaining architecture and identity. The fourth international conference for Heritage conservation, sustainable heritage: global vision, local experience, Doha, Qatar.

[4] Xu, J., Ding, L. and Love, P. E. D. (2017). Digital reproduction of historical building ornamental components: From 3D scanning to 3D printing. Autom. Constr., Amsterdam, Netherlands, pp. 85–96. DOI: 10.1016/j.autcon.2017.01.010.

[5] Higueras, M., Calero, A. I. and Collado-Montero, F. J. (2021). Digital 3D modeling using photogrammetry and 3D

printing applied to the restoration of a Hispano-Roman architectural ornament. Digit. Appl. Archaeol. Cult. Herit., Barcelona, Spain, pp. e00179. DOI: 10.1016/j.daach.2021.e00179.

[6] Papas, N., Tsongas, K. and Karolidis, D. (2023). The integration of 3D technologies and finite element analysis (FEA) for the restoration of an ancient terra sigillata plate. Digit. Appl. Archaeol. Cult. Herit., Athens, Greece, pp. e00260. DOI: 10.1016/j.daach.2023.e00260.

[7] Monaldo, E., Ricci, M. and Marfia, S. (2023). Mechanical properties of 3D printed polylactic acid elements: Experimental and numerical insights. Mech. Mater., Oxford, UK, pp. 104551. DOI: 10.1016/j.mechmat.2022.104551.

[8] Tanikella, N. G., Wittbrodt, B. and Pearce, J. M. (2017). Tensile strength of commercial polymer materials for fused filament fabrication 3D printing. Addit. Manuf., Amsterdam, Netherlands, pp. 40–47. DOI: 10.1016/j.addma.2017.02.001.

[9] Song, Y., Li, Y. and Song, W. (2017). Measurements of the mechanical response of unidirectional 3D-printed PLA. Mater. Des., Amsterdam, Netherlands, pp. 154–164. DOI: 10.1016/j.matdes.2017.03.072.

[10] Yao, T., Ye, J. and Deng, Z. (2020). Tensile failure strength and separation angle of FDM 3D printing PLA material: Experimental and theoretical analyses. Compos. Part B Eng., Amsterdam, Netherlands, pp. 107894. DOI: 10.1016/j.compositesb.2020.107894.

[11] Hack, N., Lindemann, H. and Kloft, H. (2019). Adaptive modular spatial structures for shotcrete 3D printing. Intell. Inf. - Proc. 24th Int. Conf. Comput. Archit. Des. Res. Asia, CAADRIA 2019, Hong Kong, China, pp. 363–372.

[12] Dörrie, R., Zimmermann, L. and Hampel, F. (2023). Automated force-flow-oriented reinforcement integration for Shotcrete 3D Printing. Autom. Constr., Amsterdam, Netherlands, pp. 105075. DOI: 10.1016/j.autcon.2023.105075.

[13] Palaniyappan, S., Annamalai, G. and Sivakumar, N. K. (2023). Development of functional gradient multi-material composites using Poly Lactic Acid and walnut shell reinforced Poly Lactic Acid filaments by fused filament fabrication technology. J. Build. Eng., New York, NY, pp. 105746. DOI: 10.1016/j.jobe.2023.105746.

[14] Fico, D., Rizzo, D. and De Carolis, V. (2022). Development and characterization of sustainable PLA/Olive wood waste composites for rehabilitation applications using Fused Filament Fabrication (FFF). J. Build. Eng., New York, NY, pp. 104673. DOI: 10.1016/j.jobe.2022.104673.

[15] Tomei, V., Grande, E. and Caponero, M. A. (2024). 3D-printing for the rehabilitation and health monitoring of structures with FBG: Experimental tests. Constr. Build. Mater., Amsterdam, Netherlands, pp. 135067. DOI: 10.1016/j.conbuildmat.2023.135067.

[16] Yao, T., Deng, Z. and Zhang, K. (2019). A method to predict the ultimate tensile strength of 3D printing polylactic acid (PLA) materials with different printing orientations. Compos. Part B Eng., Amsterdam, Netherlands, pp. 393–402. DOI: 10.1016/j.compositesb.2018.09.061.

[17] Wittbrodt, B. and Pearce, J. M. (2015). The effects of PLA color on material properties of 3-D printed components. Addit. Manuf., Amsterdam, Netherlands, pp. 110–116. DOI: 10.1016/j.addma.2015.03.006.

[18] Letcher, T. and Waytashek, M. (2014). Material Property Testing of 3D-Printed Specimen in PLA on an Entry-Level 3D Printer. Addit. Manuf., Amsterdam, Netherlands.

[19] Tedeschi, A. (2014). AAD Algorithms-Aided Design: Parametric Strategies Using Grasshopper. New York, NY.

[20] Rutten, D. (2007). Grasshopper: generative modeling for Rhino. Robert McNeel & Associates, Seattle, WA.

[21] Preisinger, C. (2019). Karamba3D. Bollinger und Grohmann ZT GmbH, Vienna, Austria.

[22] Bellini, C., Berto, F. and Di Cocco, V. (2021). Additive manufacturing processes for metals and effects of defects on mechanical strength: a review. Procedia Struct. Integr., Amsterdam, Netherlands, pp. 498–508. DOI: 10.1016/j.prostr.2021.03.064.

[23] Mourad, A. H. I., Khaliq, J. and Hamad, K. (2019). Mechanical Performance Assessment of Internally-Defected Materials Manufactured Using Additive Manufacturing Technology. J. Manuf. Mater. Process., Basel, Switzerland, pp. 74. DOI: 10.3390/jmmp3030074.

[24] Smith, M. (2023). ABAQUS/Standard User's Manual, Version 2023. Dassault Systèmes Simulia Corp., United States.